

Contents lists available at ScienceDirect

Petroleum Science

journal homepage: www.keaipublishing.com/en/journals/petroleum-science



Original Paper

Far-field radiation patterns of distributed acoustic sensing in anisotropic media with an explosive source and vertically straight fiber



Le-Le Zhang ^a, Yang Zhao ^{a, *}, Lu Liu ^b, Ge Jin ^c, Cheng-Gang Xian ^a, Zhi-Peng Ning ^a, Chuang-Yang Wang ^a

- ^a State Key Laboratory of Petroleum Resource and Engineering, Unconventional Petroleum Research Institute, China University of Petroleum (Beijing), Beijing, 102249, China
- ^b Aramco Beijing Research Center, Aramco Asia, Beijing, 100102, China
- ^c Colorado School of Mines, Department of Geophysics, 1500 Illinois St, Golden, CO, 80401, USA

ARTICLE INFO

Article history: Received 13 May 2024 Received in revised form 7 September 2024 Accepted 9 October 2024 Available online 11 October 2024

Edited by Meng-Jiao Zhou and Jie Hao

Keywords:
Distributed acoustic sensing
Seismic anisotropy
Geophysical methods
Numerical solutions

ABSTRACT

Distributed acoustic sensing (DAS) is increasingly used in seismic exploration owing to its wide frequency range, dense sampling and real-time monitoring. DAS radiation patterns help to understand angle response of DAS records and improve the quality of inversion and imaging. In this paper, we solve the 3D vertical transverse isotropic (VTI) Christoffel equation and obtain the analytical, first-order, and zero-order Taylor expansion solutions that represent P-, SV-, and SH-wave phase velocities and polarization vectors. These analytical and approximated solutions are used to build the P/S plane-wave expression identical to the far-field term of seismic wave, from which the strain rate expressions are derived and DAS radiation patterns are thus extracted for anisotropic P/S waves. We observe that the gauge length and phase angle terms control the radiating intensity of DAS records. Additionally, the Bond transformation is adopted to derive the DAS radiation patterns in title transverse isotropic (TTI) media, which exhibits higher complexity than that of VTI media. Several synthetic examples demonstrate the feasibility and effectiveness of our theory.

© 2024 The Authors. Publishing services by Elsevier B.V. on behalf of KeAi Communications Co. Ltd. This is an open access article under the CC BY-NC-ND license (http://creativecommons.org/licenses/by-nc-nd/

4.0/).

1. Introduction

Distributed acoustic sensing (DAS) has grown rapidly both in theory development and industrial applications (Willis, 2022). Because of the heterogeneous properties in optical fiber materials, DAS can utilize Rayleigh backscattered waves to demodulate phase changes and generate strain response. At present, DAS technology has been widely applied in vertical seismic profile (VSP) reservoir prediction (Mateeva et al., 2014; Zhan and Nahm, 2020), microseismic monitoring (Eaid et al., 2018; Li and Jin, 2024), near-surface characterization (Dou et al., 2017; Lellouch et al., 2021) and full waveform inversion (Egorov et al., 2018; Eaid et al., 2020). Because the optical fiber material is cost-friendly, researchers can deploy a long-distance array (the approximated limit equals half traveling

distance of light pulse within the transmitting time interval of light pulse) and obtain highly dense DAS sampling data. Moreover, the optical fiber is more feasible than geophones in downhole environments

Although DAS technology exhibits huge potential in exploration, there are also some challenges. Different from 3-C geophones, straight optical fibers are sensitive to the deploying direction, which only can receive single strain component. Perpendicular incident or polarized (taking optical fiber deploying direction as reference) waves are hard to be detected. To solve this problem, helical winding fibers are designed to receive the projections of all strain field components (Ning and Sava, 2018; Zhang et al., 2024). However, the radiation patterns of strain rate records via both straight and helical fibers are rarely analyzed especially in anisotropic media, which can supply an important theory basis for inversion or imaging. For instance, the radiation patterns present the amplitude intensity of P- and S-wave varying with incident angle in DAS data, which indicates the illumination energy range

E-mail address: zhaoyangprof1@qq.com (Y. Zhao).

^{*} Corresponding author.

for seismic imaging and associated angle gathers in the given geometry. Aki and Richards (2002) derived the displacement expression with seismology moment tensor in isotropic media. They utilize Helmholtz decomposition and sphere symmetry theory to solve the near-, mid-, and far-field displacement terms of elastic waves. Following their work. Rodriguez and Wuestefeld (2020) developed the radiation patterns of DAS for microseismic events in isotropic media. However, in anisotropic media, the polarization direction is different from the wave propagating direction (Tsvankin, 2012), and phase velocity varies with incident angles. Conventional Helmholtz decomposition can not be used to solve the anisotropic elastic equation and to obtain the radiation patterns formula. To address this problem, the Christoffel equation in anisotropic media can be built and supply the eigenvalue and eigenvectors as phase velocity and polarization vector, which are widely applied in exploration (Dellinger and Etgen, 1990; Yang et al., 2019; Zhang et al., 2022, 2023a).

In this paper, we focus on the explosive point source, which provides scalar amplitude for elastic waves in anisotropic media. We first solve the 3D VTI Christoffel equation and obtain P-, SV-, and SH-wave phase velocity and their associated polarization vectors. These solutions are used to build the P/S plane-wave displacement expression in homogeneous anisotropic media, corresponding to elastic wave far-field term. The strain rate formulations and radiation patterns via an explosive source for straight optical fiber are then derived. Moreover, Bond transformation is used to convert the strain rate expression from VTI to TTI media. The synthetic examples demonstrate the feasibility and effectiveness of our theory.

2. Methodology

2.1. Radiation patterns for P/S wave displacement in 3D VTI media

The radiation patterns RD for P-, SV- and SH-wave displacement

in 3D VTI media with an explosive source can be given by (see detailed derivations in Appendix A)

$$\mathbf{RD}_{P} = \frac{\mathbf{D}^{P}}{\left|\mathbf{D}^{P}\right|} = \frac{(l, m, r^{p}n)}{\sqrt{l^{2} + m^{2} + (r^{p})^{2}n^{2}}},$$

$$\mathbf{RD}_{SV} = \frac{\mathbf{D}^{SV}}{\left|\mathbf{D}^{SV}\right|} = \frac{\left(r^{sv}ln, r^{sv}mn, l^{2} + m^{2}\right)}{\sqrt{\left(l^{2} + m^{2}\right)\left(l^{2} + m^{2} + (r^{sv})^{2}n^{2}\right)}},$$

$$\mathbf{RD}_{SH} = \frac{\mathbf{D}^{SH}}{\left|\mathbf{D}^{SH}\right|} = \frac{(m, -l, 0)}{\sqrt{l^{2} + m^{2}}},$$
(1)

where \mathbf{D}^{P} , \mathbf{D}^{SV} and \mathbf{D}^{SH} are polarization vector of P-, SV-, SH-wave, respectively, which expression can be found in Appendix A. The l, m, n represent the wave propagating direction and are expressed as

$$l = \sin(\theta)\cos(\psi),$$

$$m = \sin(\theta)\sin(\psi),$$

$$n = \cos(\theta),$$
(2)

where θ and ψ are the phase angles of elastic waves in the 3D space. For the horizontal interface (dip angle equals zero), they can be called incident (θ) and azimuth (ψ) angle. r is the weighted model coefficients. $r^{\rm p}$ and $r^{\rm sv}$ can be expressed with an analytical solution (Eq. (A-17)) as

$$\begin{split} r^p &= \frac{\sqrt{\left[(1+2\delta)v_p^2 - v_s^2\right]\left(v_p^2 - v_s^2\right)}\left(l^2 + m^2\right)}{f_1(\theta) - \left(v_s^2\left(l^2 + m^2\right) + v_p^2n^2\right)} \\ f_1(\theta) &= \left[\left((1+2\epsilon)v_p^2 + v_s^2\right)\left(l^2 + m^2\right) + \left(v_p^2 + v_s^2\right)n^2\right] / 2 + \left[\left((1+2\epsilon)v_p^2 - v_s^2\right)\left(l^2 + m^2\right) + \left(v_p^2 - v_s^2\right)n^2\right] / 2 \times \\ \sqrt{1 + \frac{8(\delta - \epsilon)v_p^2\left(v_p^2 - v_s^2\right)\left(l^2 + m^2\right)n^2}{\left[\left((1+2\epsilon)v_p^2 - v_s^2\right)\left(l^2 + m^2\right) + \left(v_p^2 - v_s^2\right)n^2\right]^2}}, \\ r^{sv} &= \frac{\sqrt{\left[(1+2\delta)v_p^2 - v_s^2\right]\left(v_p^2 - v_s^2\right)\left(l^2 + m^2\right)}}{f_2(\theta) - \left((1+2\epsilon)v_p^2\left(l^2 + m^2\right) + v_s^2n^2\right)} \\ f_2(\theta) &= \left[\left((1+2\epsilon)v_p^2 + v_s^2\right)\left(l^2 + m^2\right) + \left(v_p^2 - v_s^2\right)\left(l^2 + m^2\right) + \left(v_p^2 - v_s^2\right)n^2\right] / 2 \times \\ \sqrt{1 + \frac{8(\delta - \epsilon)v_p^2\left(v_p^2 - v_s^2\right)\left(l^2 + m^2\right)n^2}{\left[\left((1+2\epsilon)v_p^2 - v_s^2\right)\left(l^2 + m^2\right) + \left(v_p^2 - v_s^2\right)n^2\right]^2}} \end{split}$$

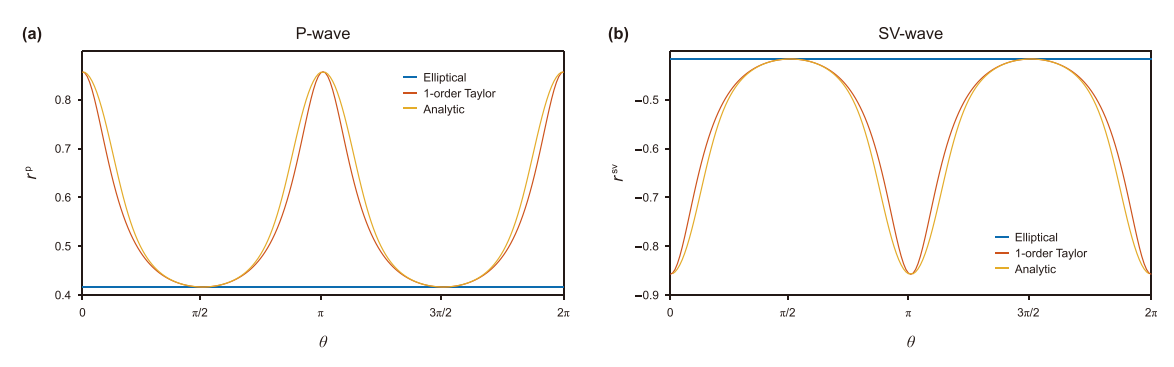


Fig. 1. The r^p and r^{sv} curves with three solutions. Panel (a) r^p curve for P-wave data, and (b) r^{sv} curve for SV-wave data.

and with first-order Taylor expansion solution (Eq. (A-18)) as

polarization vector and seismic imaging (Zhang and McMechan,

$$\begin{split} r^{p} &= \frac{\sqrt{\left[(1+2\delta)\nu_{p}^{2}-\nu_{s}^{2}\right]\left(\nu_{p}^{2}-\nu_{s}^{2}\right)}}{\left[(1+2\epsilon)\nu_{p}^{2}-\nu_{s}^{2}\right]+2(\delta-\epsilon)\nu_{p}^{2}\left(\nu_{p}^{2}-\nu_{s}^{2}\right)n^{2}/\left[\left((1+2\epsilon)\nu_{p}^{2}-\nu_{s}^{2}\right)\left(l^{2}+m^{2}\right)+\left(\nu_{p}^{2}-\nu_{s}^{2}\right)n^{2}\right]},\\ r^{sv} &= \frac{\sqrt{\left[(1+2\delta)\nu_{p}^{2}-\nu_{s}^{2}\right]\left(\nu_{p}^{2}-\nu_{s}^{2}\right)}}{\left[\nu_{s}^{2}-(1+2\epsilon)\nu_{p}^{2}\right]-2(\delta-\epsilon)\nu_{p}^{2}\left(\nu_{p}^{2}-\nu_{s}^{2}\right)n^{2}/\left[\left((1+2\epsilon)\nu_{p}^{2}-\nu_{s}^{2}\right)\left(l^{2}+m^{2}\right)+\left(\nu_{p}^{2}-\nu_{s}^{2}\right)n^{2}\right]}, \end{split} \tag{4}$$

and with elliptical assumption solution (Eq. (A-19)) as

$$r^{\rm p} = -r^{\rm sv} = \frac{\sqrt{\left[(1+2\delta)v_{\rm p}^2 - v_{\rm s}^2\right]\left[v_{\rm p}^2 - v_{\rm s}^2\right]}}{(1+2\epsilon)v_{\rm p}^2 - v_{\rm s}^2},\tag{5}$$

where v_p and v_s are vertical P- and S-wave velocity, respectively. ϵ and δ are anisotropic parameters. Eq. (1) indicates that the radiation patterns mainly depend on the phase angles θ and ψ and model parameters r^p and r^{sv} . Eqs. (3)–(5) are commonly served for

2010; Cheng and Fomel, 2014; Yang et al., 2019; Zhang et al., 2022). Therefore, radiation patterns can be used here to exhibit the difference among these approximated and accurate solutions.

2.2. Modeling test for VTI displacement radiation patterns

The radiation patterns test of P/S wave displacement is performed on a 3D VTI homogeneous model. The P- and S-wave velocities are set as 3000 and 2000 m/s, respectively. The density is 2 g/cm^3 . The anisotropic parameters ϵ , δ and γ are 0.5, 0.1, and 0.5, respectively. Fig. 1 shows the coefficient r^{p} and r^{sv} curves with

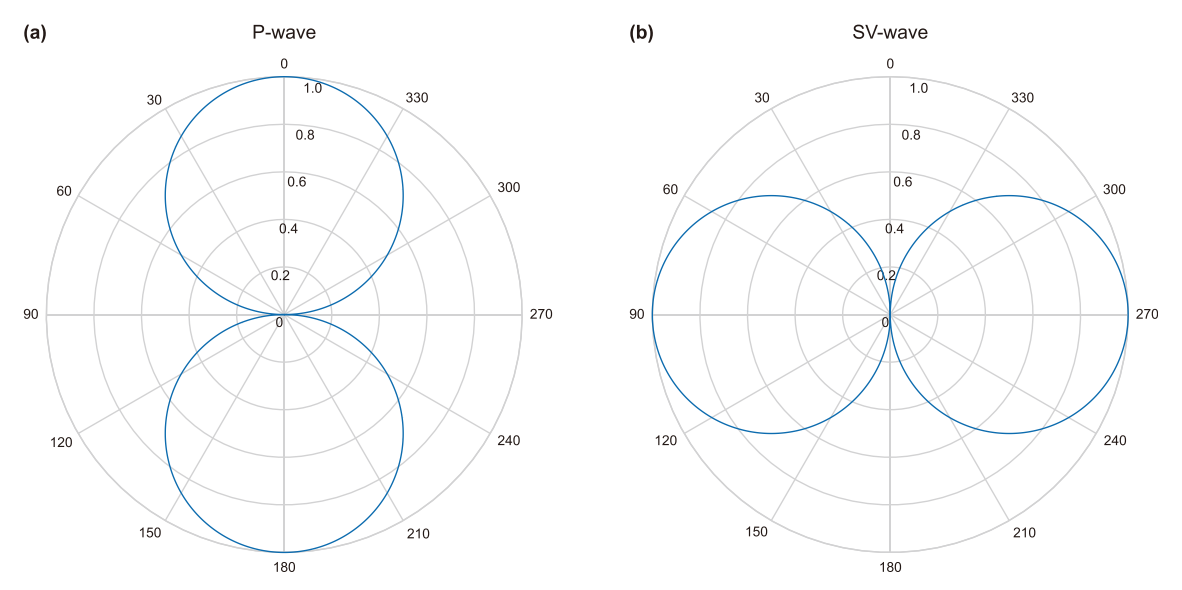


Fig. 2. Radiation patterns of **(a)** P- and **(b)** SV-wave displacement in isotropic media from 0° to 360°.

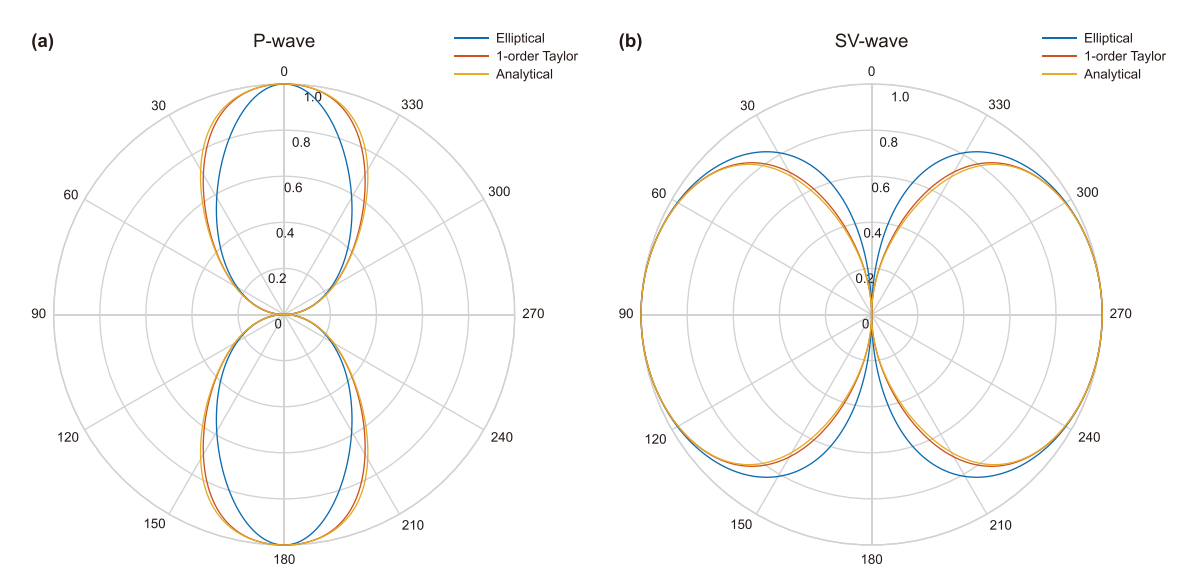


Fig. 3. Radiation patterns of (a) P- and (b) SV-wave displacement in VTI media from 0° to 360°.

different solutions (Eqs. (3)–(5)). The first-order Taylor expansion and analytical solutions share a similar variation with the period of π . The elliptical solution is a constant line and tangent to peak points of two other curves at incident angles of $\pi/2$ and $3\pi/2$. This happens due to n=0 at $\theta=\pi/2$ and $3\pi/2$ in Eqs. (3) and (4). For other non-tangent points, the elliptical solution exhibits some inevitable errors compared with the analytical result, which can influence the radiation patterns. In this paper, we suppose the straight optical fiber deployed in a vertical wellbore, and the zcomponents of displacement or strain are thus detected. The reason we choose vertical wellbore direction is that $r^p n$ and $l^2 + m^2$ in Eq. (1) (z-components) only include phase angle θ which determines the anisotropic characteristics in VTI media (Anisotropy in VTI media is independent of phase angle ψ). Meantime, note that $u_z^{\rm sh} =$ 0 in Eq. (1). This will not lose anisotropic information because the polarization of the SH-wave is isotropic.

Fig. 2 is the isotropic (set $r^p = 1$ and $r^{sv} = -1$ in Eq. (1)) radiation patterns of P- and SV-wave displacement, which shows a sin and cos function characteristics, respectively. Adopting three solutions

inversion in the strong non-elliptical area may encounter inevitable errors.

2.3. Radiation patterns of DAS response in 3D VTI media

Different from geophone data which detects displacement (or velocity) signal, the DAS records convert the phase change of pulse light to strain rate. Suppose we deploy the straight optical fiber in a vertical wellbore, the DAS response can be expressed as (Willis, 2022)

$$\dot{\epsilon}_{\rm d} = \frac{1}{GL} \frac{\partial}{\partial t} \int_{z-GL/2}^{z+GL/2} \frac{\partial u_z}{\partial z} dz = \frac{\partial}{\partial t} \frac{u_z(z+GL/2) - u_z(z-GL/2)}{GL}$$
 (6)

where $\epsilon_{\rm d}$ represents the strain rate for DAS records, *GL* is the gauge length, u_z represents the *z*-components of displacement.

By substituting Eq. (A-21) into Eq. (6), we can obtain the strain rate of P- and SV-wave as

$$\dot{\epsilon}_{p} = \frac{2\omega A_{0}}{GL} \frac{rn}{\sqrt{l^{2} + m^{2} + r^{2}n^{2}}} \sin\left(\frac{\omega}{V_{P}} \frac{GL}{2}n\right) e^{-i\omega(t - \frac{1}{V_{P}}(xl + ym + zn))},$$

$$\dot{\epsilon}_{sv} = \frac{2\omega A_{0}}{GL} \frac{\left(l^{2} + m^{2}\right)}{\sqrt{l^{2} + m^{2}}\sqrt{l^{2} + m^{2} + r^{2}n^{2}}} \sin\left(\frac{\omega}{V_{SV}} \frac{GL}{2}n\right) e^{-i\omega(t - \frac{1}{V_{SV}}(xl + ym + zn))},$$

$$(7)$$

(Eqs. (3)–(5)), radiation patterns of VTI P-wave (Fig. 3(a)) are shrunk to a quasi-elliptical curve but with the same maximum value at incident angle $\theta=0^\circ$ (due to symmetry, we only require to focus on phase angle θ from 0° to 90°). In contrast, the radiation patterns of VTI SV-wave are expanded to a quasi-elliptical which covers the radiating range of isotropic media with the same maximum value position at incident angle $\theta=90^\circ$. In addition, the elliptical solution is different from first-order Taylor expansion and analytical curves. Some researches using elliptical assumptions to perform angle gathers extraction or amplitude versus angle (AVA)

Because we deploy a vertical optical fiber in the well, there are no z-components of SH-wave detected. This is applicable because we main focus on the explosive source exploration, which give a weak energy of SH-wave. The x- and y-components of P-, SV- and SH-wave can be obtained by deploying the optical fiber in the ground along the x-axis and y-axis, respectively. The derivation is similar to Eqs. (6) and (7), which only need to replace the z-with the x-axis or y-axis and associated polarization components.

From Eq. (7) we can extract the radiation patterns of DAS strain rate records for P- and SV-wave z-components as

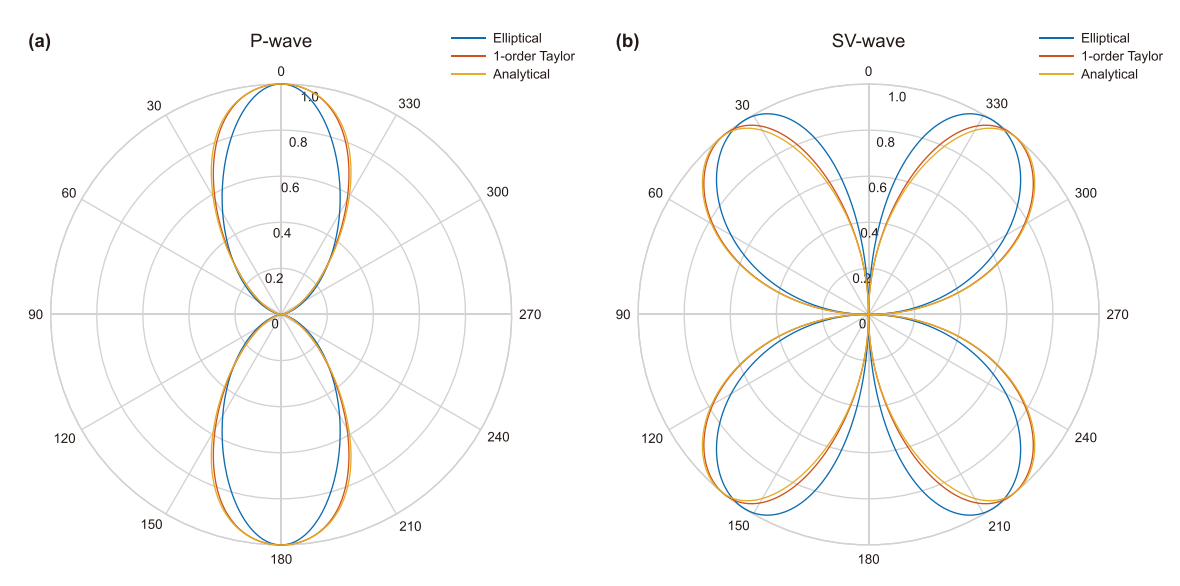


Fig. 4. Radiation patterns of (a) P- and (b) SV-wave for DAS strain rate in VTI media from 0° to 360°.

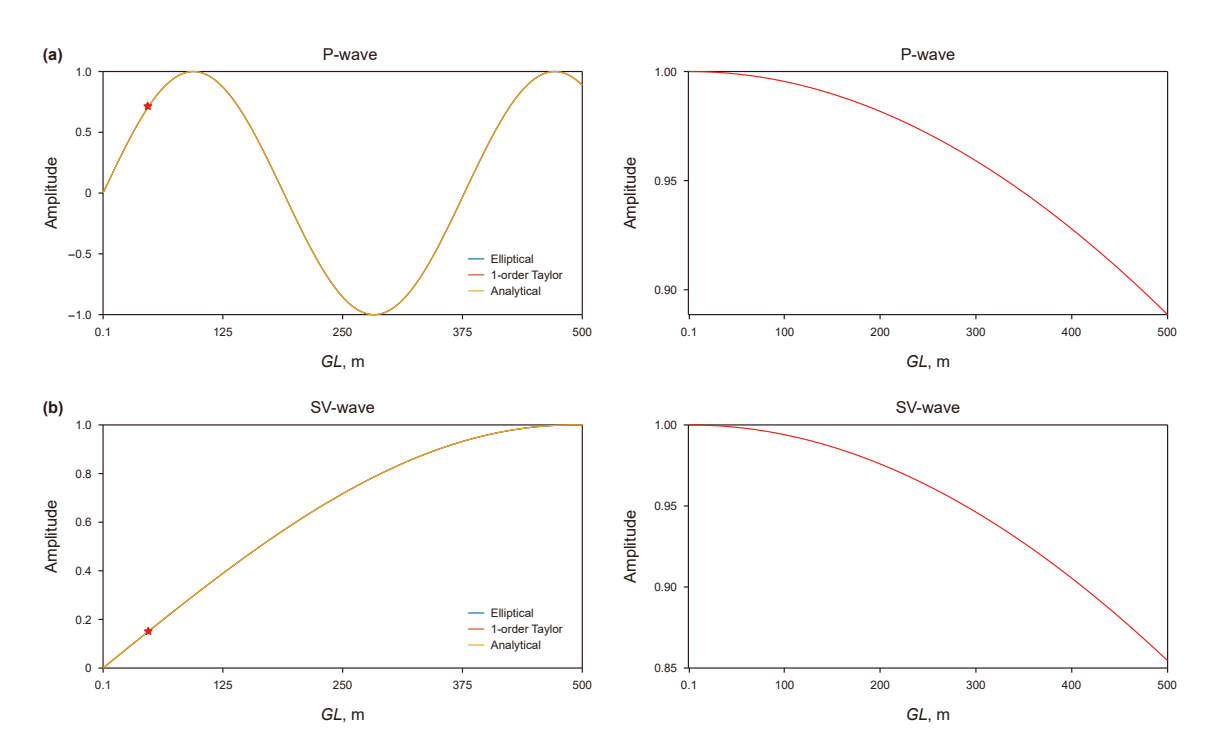


Fig. 5. Radiating amplitude variation of (a) P- and (b) SV-wave for DAS response in VTI media with the increasing of gauge length from 0 m to 500 m.

$$\begin{split} RS_{Pz} &= \frac{1}{GL} \frac{r^p n}{\sqrt{l^2 + m^2 + (r^p)^2 n^2}} sin \left(\frac{\omega}{V_P} \frac{GL}{2} n\right), \\ RS_{SVz} &= \frac{1}{GL} \frac{\left(l^2 + m^2\right)}{\sqrt{l^2 + m^2} \sqrt{l^2 + m^2 + (r^{sv})^2 n^2}} sin \left(\frac{\omega}{V_{SV}} \frac{GL}{2} n\right), \end{split} \tag{8}$$

where V_P and V_{SV} are P- and SV-wave phase velocity, which can be found in Appendix A. Note V_P , V_{SV} , r^P and r^{SV} are the function of model parameters and θ . Therefore, for the homogeneous media, the DAS radiation patterns of P- and SV-wave (Eq. (8)) mainly depend on incident angle θ and gauge length GL.

Keeping the model parameters unchanged as modeling test in VTI displacement radiation patterns section and setting ω as $10\times2\pi$ Hz and GL as 4 m, Fig. 4 shows the DAS radiation patterns of VTI P-and SV-wave. Compared with Fig. 3, the radiating range of the DAS P-wave (Fig. 4(a)) further decreases and the elliptical solution is surrounded by the analytical curve. More interestingly, the DAS radiation patterns of SV-wave (Fig. 4(b)) are totally changed to quadrangular petal, and the maximum value position varies from 90° to 33° (elliptical solution) and 40° (analytical solution). These indicate the P- and SV-waves in DAS records possess a smaller illustration range than that of geophone data. Then, we fix the incident angle $\theta=0^{\circ}$ for P-wave and $\theta=40^{\circ}$ for SV-wave to show the radiation amplitude variation (Eq. (8)) with the increasing of gauge length GL (Fig. 5). The P- and SV-wave velocity are calculated

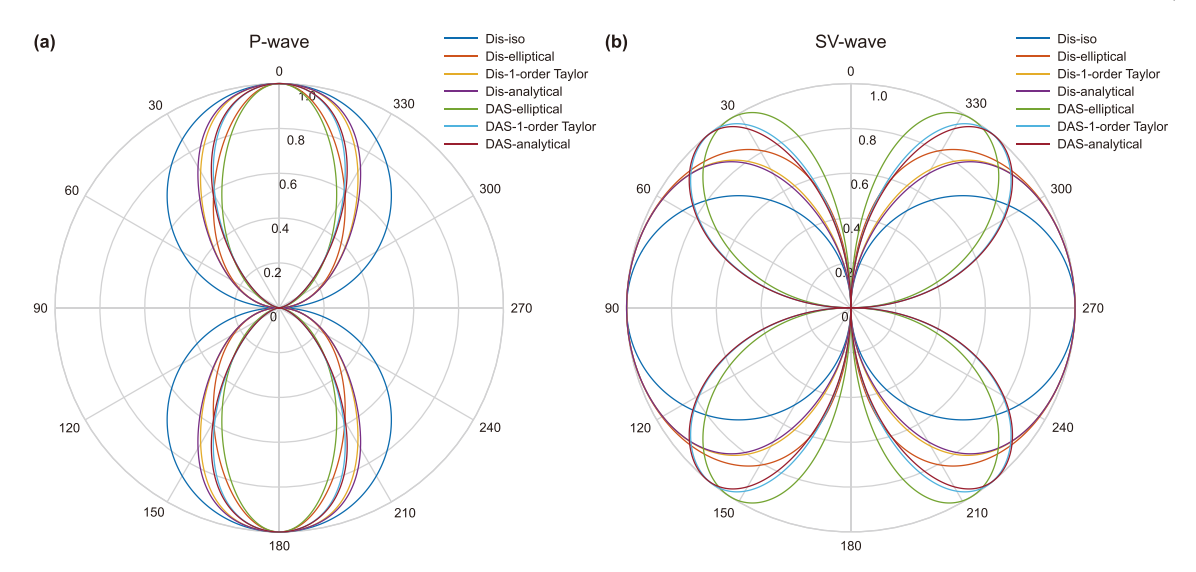


Fig. 6. Radiation patterns of (a) P- and (b) SV-wave for displacement and DAS strain rate in isotropic and VTI media from 0° to 360° .

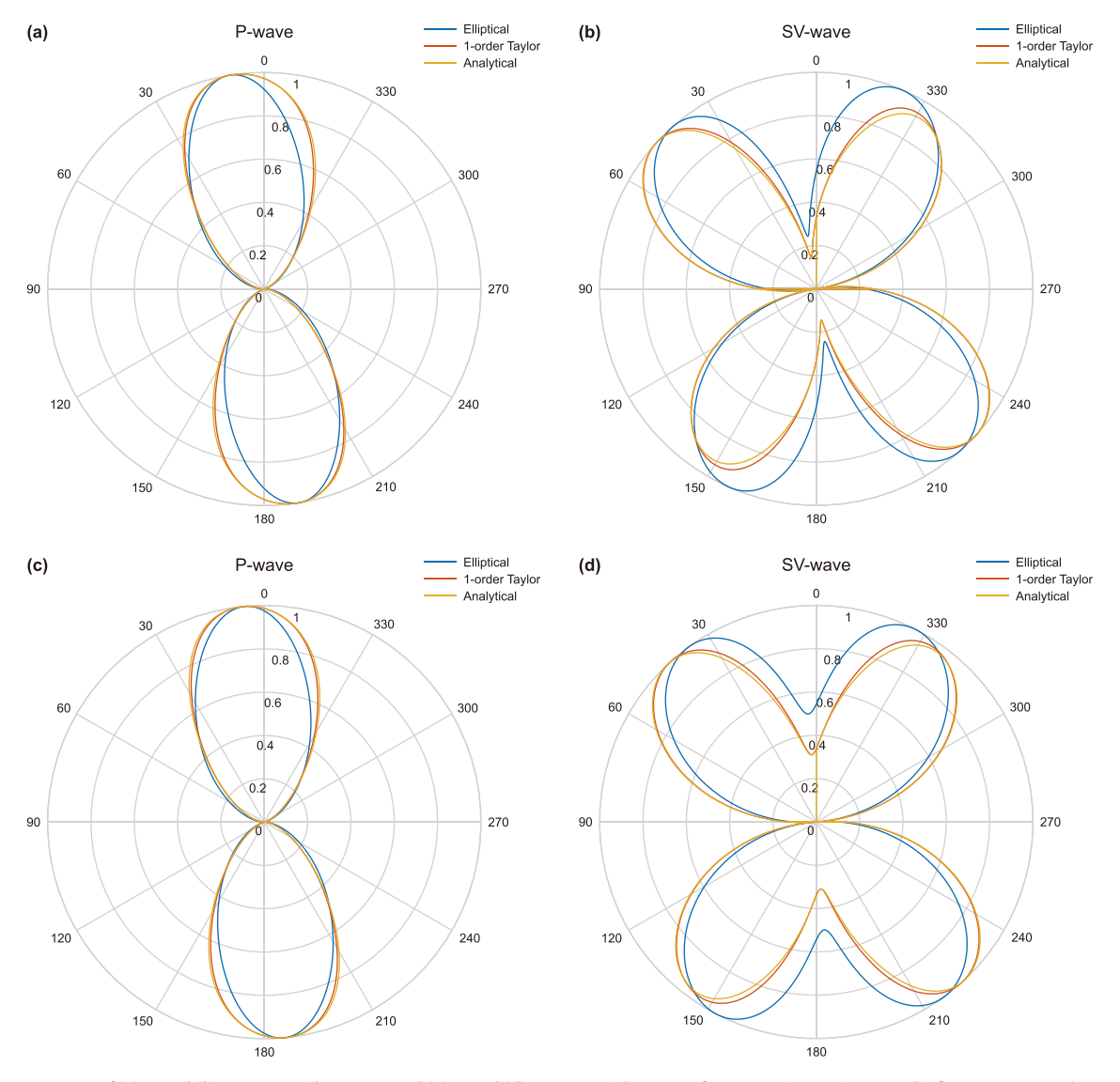


Fig. 7. Radiation patterns of **(a)** P- and **(b)** SV-wave with $\psi = 25^{\circ}$, and **(c)** P- and **(d)** SV-wave with $\psi = 65^{\circ}$ for DAS strain rate in TTI media from 0° to 360° . The rotating angle is $\theta' = 10^{\circ}$.

from Eq. (A-12). Unexpectedly, both P- and SV-wave curves do not present sin function features even if we increase the gauge length from 0.1 to 500 m. This is caused by weight term 1/GL and small seismic data frequency ω (compared with P/S wave velocity). Therefore, large gauge length usually means a smaller value in Eq. (8) and thus attenuates DAS radiating amplitudes. However, the geophone data frequency band is between 5 and 300 Hz. So that ω cannot balance the magnitude order of velocity V in term $\sin(\frac{\omega}{V}\frac{GL}{2}n)$. While the detecting frequency range of DAS itself can change from 0.1 Hz to 10000 Hz. Some other ultra-high frequency investigations may not follow the analysis in Fig. 5.

For a straight comparison, we assemble all the radiation pattern curves in Fig. 6. As observed, from isotropic to anisotropic media (for displacement), the P-wave radiation range decreases, while the SV-wave radiating range increases. From displacement to DAS records (strain rate), both P- and SV-wave radiation patterns shrink and especially SV-wave range becomes very narrow (quadrangular petal). This indicates a disadvantage for DAS in seismic inversion and migration because we have to use fewer incident angle information than that of geophone data.

2.4. Radiation patterns of DAS response in 3D TTI media

Bond transformation (Yang et al., 2019; Zhang et al., 2023a) can be used to convert VTI to TTI media, which is identical to coordinate rotation on wavenumber components. Setting the *y*-axis as the rotating axis, we can obtain the coordinate transform formation in 3D TTI media as

$$\begin{bmatrix} l' \\ m' \\ n' \end{bmatrix} = \begin{bmatrix} \cos(\theta') & 0 & \sin(\theta') \\ 0 & 1 & 0 \\ -\sin(\theta') & 0 & \cos(\theta') \end{bmatrix} \begin{bmatrix} l \\ m \\ n \end{bmatrix}$$
$$= \begin{bmatrix} \cos(\theta')l + \sin(\theta')n \\ m \\ -\sin(\theta')l + \cos(\theta')n \end{bmatrix}, \tag{9}$$

where θ' represents the rotating angle between the *z*-axis and symmetry axis of TTI media. By replacing l, m, n of Eq. (8) with l', m', n' of Eq. (9), we obtain the radiation patterns of DAS records with vertical optical fiber in TTI media as

(for analytical solution curve) and 36.6° (for elliptical solution curve). The change of angle position for maximum value (from Figs. 4–7) is close to the rotating angle θ' . Then we increase the ψ to 65° , the maximum position for the P-wave is changed to 5.94° (for analytical solution curve) and 5.4° (for elliptical solution curve) and for SV-wave data is changed to 43.2° and 36.18° . The rotating extent of maximum positions slows down with the development of phase angle ψ , which indicates the radiation patterns are also influenced by phase angle ψ in TTI media.

3. Discussion

To start with, this paper solves the 3D VTI Christoffel equation to obtain three types of analytical, first-order, and zero-order (elliptical assumption) Taylor expansion solutions which represent P-, SV- and SH-wave polarization vectors, respectively. As observed in Figs. 3, 4 and 7, the analytical and first-order Taylor solution present same accuracy, and exhibit a little difference compared with elliptical solution under the obvious non-elliptical condition (ϵ = 0.5, δ = 0.1). However, most common rocks (such as sedimentary rocks) present weak anisotropy. The elliptical assumption (Eqs. (A-14) and (A-19)) is sufficient to fulfill the requirement of seismic imaging and inversion, which possess huge advantage in efficiency (Yang et al., 2019; Zhang et al., 2022, 2023a; Zuo et al., 2022).

A plane-wave expression is proposed via calculated polarization and scalar source for anisotropic P/S waves. However, we only derive the far-field term for displacement which is suitable for seismic exploration. For hydraulic engineering, the near-field term is dominant in DAS response. In anisotropic media, deriving a near-field term is very difficult due to the many model parameters (five elastic and anisotropic models parameters in VTI media) in elastic wave equation. Here we give a near-field expression of DAS data for simple isotropic case ($\epsilon = \delta = 0$). According to Vavrycuk (2001), Aki and Richards (2002) and Vavrycuk (2007), the near-field term for isotropic displacement with a point source can be expressed as

$$u^{\text{lon}} = \frac{p}{2\pi\rho r_0^3} \int_{t1}^{t2} \tau X(t-\tau) d\tau,$$

$$u^{\text{trs}} = \frac{q}{2\pi\rho r_0^3} \int_{t1}^{t2} \tau X(t-\tau) d\tau,$$
(11)

$$RS_{Pz} = \frac{1}{GL} \frac{r^{p}(-\sin(\theta')l + \cos(\theta')n)}{f_{1}(l,m,n)} \sin\left(\frac{\omega}{V_{P}} \frac{GL}{2}(-\sin(\theta')l + \cos(\theta')n)\right),$$

$$f_{1}(l,m,n) = sqrt\left(\left(\cos^{2}\left(\theta'\right) + (r^{p})^{2}\sin^{2}\left(\theta'\right)\right)l^{2} + m^{2} + \left(\sin^{2}\left(\theta'\right) + (r^{p})^{2}\cos^{2}\left(\theta'\right)\right)n^{2} + 2\left(1 - (r^{p})^{2}\right)\cos\left(\theta'\right)\sin\left(\theta'\right)ln\right),$$

$$RS_{SVz} = \frac{1}{GL} \frac{(\cos(\theta')l + \sin(\theta')n)^{2} + m^{2}}{f_{2}(l,m,n)} \sin\left(\frac{\omega}{V_{SV}} \frac{GL}{2}(-\sin(\theta')l + \cos(\theta')n)\right),$$

$$f_{2}(l,m,n) = \sqrt{(\cos(\theta')l + \sin(\theta')n)^{2} + m^{2}}\sqrt{(\cos(\theta')l + \sin(\theta')n)^{2} + m^{2} + (r^{SV})^{2}(-\sin(\theta')l + \cos(\theta')n)^{2}},$$

$$(10)$$

Compared with Eq. (8), the DAS radiation patterns expression becomes more complex in TTI media (Eq. (10)) due to one more variable θ' . Using same numerical test parameters in VTI DAS radiation patterns example and setting the rotating angle $\theta'=10^\circ$ in Eq. (10), we plot the DAS radiation patterns of TTI media in Fig. 7. Compared with Fig. 4, the whole radiating shape rotates toward to left side. For $\psi=25^\circ$ set in Fig. 6(a) and (b), the maximum value position of P-wave data are 8.64° (for analytical solution curve) and 9.36° (for elliptical solution curve), and for SV-wave data are 48.24°

where, $u^{\rm lon}$ and $u^{\rm trs}$ are longitudinal and transverse component of displacement near-field term, respectively. p and q are cosine of angle between force direction of point source and P- (for p)/S-wave (for q) polarization direction. Especially, when force direction is parallel to z-axis, p and q equal to z-component of P- and S-wave polarization vector (Eq. (1)). r_0 represents propagating distance from source to receiver. X(t) is the seismic wave signal. For simplicity, we use $\partial u^{\rm lon}/\partial z$ and $\partial u^{\rm trs}/\partial z$ to approximately express the

near-field term of DAS data with a point source and vertically straight fiber as

$$\begin{split} \epsilon_{\mathsf{z}}^{\mathrm{lon}} &= \frac{\partial u^{\mathrm{lon}}}{\partial z} = \frac{-3pn}{2\pi\rho r_{0}^{4}} \int_{t1}^{t2} \tau X(t-\tau) \mathrm{d}\tau, \\ \epsilon_{\mathsf{z}}^{\mathrm{trs}} &= \frac{\partial u^{\mathrm{trs}}}{\partial z} = \frac{-3qn}{2\pi\rho r_{0}^{4}} \int_{t1}^{t2} \tau X(t-\tau) \mathrm{d}\tau. \end{split} \tag{12}$$

where $\epsilon_z^{\rm lon}$ and $\epsilon_z^{\rm tr}$ are longitudinal and transverse component of DAS data near-field term for isotropic case. $n=\partial r_0/\partial z$ has been defined in Eq. (2). By comparison of Eqs. (11) and (12), the DAS data energy declines faster with $1/r_0^4$ than that of displacement with $1/r_0^3$. For the radiation patterns of near-field from displacement data (refer to p and q), it mainly determines by the force and polarization directions. While for the near-field radiation patterns of DAS data (refer to pn and qn), it depends on propagating, polarization and force directions, which means near-field of DAS data has smaller incident angle range than that of displacement data. This is in accordance with analysis in Fig. 6.

In our research, only the explosive source is used to supply the scalar amplitude for P/S waves in anisotropic media. This means that the influence of the source for radiation patterns is omitted because force direction is not considered. To solve this problem, adopting the seismology moment tensor is effective but experiences difficulty in solving non-homogeneous wave equation ("non-homogeneous" here means adding source term in the wave equation). A straight way is to directly multiply the directional cosine of force and force arm as well as moment tensor by Eqs. (1), (8) and (10). It lacks of mathematical theory but has physical meaning because the radiation patterns in isotropic media are composed of source and polarization terms (Aki and Richards, 2002), which is similar to the situation of anisotropic media.

Straight optical fiber only can detect single component along the deployed direction. To solve this problem, helical winding-fiber is designed for receiving projections from all strain-field components with equal amplitude. The winding projecting matrix via a leastsquare solution can be used for recovering the original strain fields (Zhang et al., 2023b). Therefore, deriving the radiation patterns of helical fiber is important for multiple-DAS components seismic exploration in the future. Although this paper only derives the anisotropic radiation patterns for vertical straight fiber, it is convenient to extend to deviated and helical fiber. For the deviated fiber (i.e. place fiber along inclined well), directional derivative can be applied in Eq. (6) to calculate the strain along the deploying direction of optical fiber. For the helical fiber, the DAS response fulfills projecting relationship $\dot{\epsilon}_{\rm d} = {\bf G} \epsilon$ (where ${\bf G}$ is the projecting coefficient matrix and ε is strain field). This projecting formula can replace the term $\partial u_z/\partial z$ in integration of Eq. (6) to derive the helical fiber radiation patterns.

4. Conclusion

We derive three solutions from the 3D VTI Christoffel equation to represent the polarization of P/S waves. Then plane wave theory is combined with these polarization vectors to show the far-field displacement expression. According to the transformation from geophone data (velocity) to DAS data (strain rate), we derive the DAS response formation and extract DAS radiation patterns for P/S waves, which are the function of phase angles and gauge length. Moreover, bond transforms are adopted to extend the DAS radiation patterns to TTI media, which exhibit more complexity than that of VTI media. Several examples demonstrate the feasibility of our theory.

CRediT authorship contribution statement

Le-Le Zhang: Writing — review & editing, Writing — original draft, Visualization, Validation, Supervision, Software, Resources, Project administration, Methodology, Investigation, Funding acquisition, Formal analysis, Data curation, Conceptualization. **Yang Zhao:** Writing — review & editing, Supervision. **Lu Liu:** Writing — review & editing. **Ge Jin:** Writing — review & editing. **Cheng-Gang Xian:** Writing — review & editing. **Zhi-Peng Ning:** Writing — review & editing. **Chuang-Yang Wang:** Writing — review & editing.

Data availability

The data underlying this paper are available in the paper.

Declaration of competing interest

No potential conflict of interest was reported by the authors.

Acknowledgements

We appreciate the help of the editors and the anonymous reviewers for their comments and suggestions. These significantly improved the quality of this paper. This study is jointly supported by the National Key R&D Program of China under grant No. 2021YFA0716800.

APPENDIX A

A deriving P/S wave displacement radiation patterns in 3D VTI media

The 3D VTI wave equation can be presented as (Aki and Richards, 2002; Tsvankin, 2012)

$$\rho(\mathbf{x})\partial_{t}^{2}u_{x}(\mathbf{x},t) = [c_{11}(\mathbf{x})\partial_{x}^{2} + c_{66}(\mathbf{x})\partial_{y}^{2} + c_{44}(\mathbf{x})\partial_{z}^{2}]u_{x}(\mathbf{x},t) + [c_{11}(\mathbf{x}) - c_{66}(\mathbf{x})]\partial_{xy}^{2}u_{y} + \\ [c_{13}(\mathbf{x}) + c_{44}(\mathbf{x})]\partial_{xz}^{2}u_{z}(\mathbf{x},t),$$

$$\rho(\mathbf{x})\partial_{t}^{2}u_{y}(\mathbf{x},t) = [c_{11}(\mathbf{x}) - c_{66}(\mathbf{x})]\partial_{xy}^{2}u_{x} + [c_{66}(\mathbf{x})\partial_{x}^{2} + c_{11}(\mathbf{x})\partial_{y}^{2} + c_{44}(\mathbf{x})\partial_{z}^{2}]u_{y}(\mathbf{x},t) + \\ [c_{13}(\mathbf{x}) + c_{44}(\mathbf{x})]\partial_{yz}^{2}u_{z}(\mathbf{x},t),$$

$$\rho(\mathbf{x})\partial_{t}^{2}u_{z}(\mathbf{x},t) = [c_{13}(\mathbf{x}) + c_{44}(\mathbf{x})]\partial_{xz}^{2}u_{x}(\mathbf{x},t) + [c_{13}(\mathbf{x}) + c_{44}(\mathbf{x})]\partial_{yz}^{2}u_{y}(\mathbf{x},t) + \\ [c_{44}(\mathbf{x})\partial_{x}^{2} + c_{44}(\mathbf{x})\partial_{y}^{2} + c_{33}(\mathbf{x})\partial_{z}^{2}]u_{z}(\mathbf{x},t),$$

$$(A-1)$$

where $u_x(\mathbf{x},t)$, $u_y(\mathbf{x},t)$ and $u_z(\mathbf{x},t)$ are the x-, y- and z-components of elastic wavefields, respectively. $\rho(\mathbf{x})$ is the density. \mathbf{x} is the 3D spatial Cartesian coordinate, t is the time, ∂_x^2 , ∂_y^2 and ∂_z^2 are the second partial derivatives over x, y, and z, respectively. ∂_{xz}^2 , ∂_{xz}^2 and ∂_{xz}^2 are the mixed spatial derivatives. ∂_t^2 is the second temporal derivative. c_{ij} is the stiffness matrix of 3D VTI media, which can be alternated by elastic and Thomsen anisotropic parameters (Thomsen, 1986) as

$$\begin{split} c_{11} &= (1+2\epsilon)\rho v_{\rm p}^2, c_{33} = \rho v_{\rm p}^2, c_{44} = \rho v_{\rm s}^2, c_{66} = (1+2\gamma)\rho v_{\rm s}^2 \\ c_{13} &= \rho \sqrt{\left[(1+2\delta)v_{\rm p}^2 - v_{\rm s}^2\right] \left[v_{\rm p}^2 - v_{\rm s}^2\right]} - \rho v_{\rm s}^2, \end{split} \tag{A-2}$$

where $v_{\rm p}$ and $v_{\rm s}$ are vertical P- and S-wave velocity, respectively. ϵ , δ and γ represent the anisotropic parameters.

A plane-wave expression is adopted as the solution of Eq. (A-1) as

$$\mathbf{u} = A_0 \begin{bmatrix} U_x \\ U_y \\ U_z \end{bmatrix} \exp^{-i(\omega t - k_x x - k_y y - k_z z)}, \tag{A-3}$$

where $[U_x \ U_y \ U_z]^{\rm T}$ is the polarization vector. A_0 is the scalar amplitude of the source. k, k_x , k_y , k_z are the wavenumber and its components projecting on x, y and z direction, respectively. ω is the angular frequency. Substitute Eq. (A-3) to (A-1) and we obtain the 3D VTI Christoffel equation as

$$[\mathbf{\Gamma} - \lambda \mathbf{I}]\mathbf{U} = 0, \tag{A-4}$$

with the matrix coefficients Γ as

$$\begin{split} &\Gamma_{11} = c_{11}k_x^2 + c_{66}k_y^2 + c_{44}k_z^2, \\ &\Gamma_{22} = c_{66}k_x^2 + c_{11}k_y^2 + c_{44}k_z^2, \\ &\Gamma_{33} = c_{44}k_x^2 + c_{44}k_y^2 + c_{33}k_z^2, \\ &\Gamma_{12} = \Gamma_{21} = (c_{11} - c_{66})k_xk_y, \\ &\Gamma_{13} = \Gamma_{31} = (c_{13} + c_{44})k_xk_z, \\ &\Gamma_{23} = \Gamma_{32} = (c_{13} + c_{44})k_yk_z, \end{split} \tag{A-5}$$

where $\lambda = \rho \omega^2 = \rho k^2 V^2$ represents the eigenvalue, V is the phase velocity. According to previous studies (Zhang and McMechan, 2010; Yang et al., 2019; Zhang et al., 2022), and three solutions from Eq. (4) are usually used for P/S wave decomposition and

imaging. We calculate them in this paper to show their difference in DAS radiation patterns with an explosive source. The left matrix of Eq. (A-4) is positive and has three real roots. We expand its determinant $det[\Gamma - \lambda I] = 0$ and obtain

$$\lambda^3 + a\lambda^2 + b\lambda + c = 0, (A-6)$$

with

$$\begin{split} a &= -(\Gamma_{11} + \Gamma_{22} + \Gamma_{33}) \\ b &= \Gamma_{11} * \Gamma_{22} + \Gamma_{11} * \Gamma_{33} + \Gamma_{22} * \Gamma_{33} - \Gamma_{12}^2 - \Gamma_{13}^2 - \Gamma_{23}^2, \\ c &= \Gamma_{11} * \Gamma_{23}^2 + \Gamma_{22} * \Gamma_{13}^2 + \Gamma_{33} * \Gamma_{12}^2 - \Gamma_{11} * \Gamma_{22} * \Gamma_{33} - 2 * \Gamma_{12} * \Gamma_{13} * \Gamma_{23}, \end{split}$$

Solving the cubic Eq. (A-6), we obtain three eigenvalues as

$$\begin{split} \lambda_1 &= c_{66}k_x^2 + c_{66}k_y^2 + c_{44}k_z^2, \\ \lambda_{2,3} &= \frac{1}{2} \left[(c_{11} + c_{44})k_x^2 + (c_{11} + c_{44})k_y^2 + (c_{33} + c_{44})k_z^2 \right] \pm \\ \frac{1}{2} \left[(c_{11} - c_{44})k_x^2 + (c_{11} - c_{44})k_y^2 + (c_{33} - c_{44})k_z^2 \right] \times \\ \mathrm{sqrt} \Big\{ 1 + 4 \Big(c_{11}c_{44} + c_{33}c_{44} + c_{13}^2 - c_{11}c_{33} + 2c_{13}c_{44} \Big) \Big(k_x^2 + k_y^2 \Big) k_z^2 \Big/ \\ \left[(c_{11} - c_{44})k_x^2 + (c_{11} - c_{44})k_y^2 + (c_{33} - c_{44})k_z^2 \right]^2 \Big\}, \end{split} \tag{A-8}$$

where the λ_1 , λ_2 ("+"), and λ_3 ("-") are eigenvalues for SH-, P-, and SV-waves. The sqrt represents the square root operator. Replacing the VTI stiffness matrix coefficients with Thomsen parameters (Eq. (A-2)) in Eq. (A-8), we can further obtain

$$\begin{split} &\lambda_{1} = \rho v_{s}^{2} \left[(1+2\gamma)k_{x}^{2} + (1+2\gamma)k_{y}^{2} + k_{z}^{2} \right], \\ &\lambda_{2,3} = \frac{1}{2} \left[\left((1+2\epsilon)v_{p}^{2} + v_{s}^{2} \right)k_{x}^{2} + \left((1+2\epsilon)v_{p}^{2} + v_{s}^{2} \right)k_{y}^{2} + \left(v_{p}^{2} + v_{s}^{2} \right)k_{z}^{2} \right] \pm \\ &\frac{1}{2} \left[\left((1+2\epsilon)v_{p}^{2} - v_{s}^{2} \right)k_{x}^{2} + \left((1+2\epsilon)v_{p}^{2} - v_{s}^{2} \right)k_{y}^{2} + \left(v_{p}^{2} - v_{s}^{2} \right)k_{z}^{2} \right] \times \\ & \operatorname{sqrt} \left\{ 1 + 8(\delta - \epsilon)v_{p}^{2} \left(v_{p}^{2} - v_{s}^{2} \right) \left(k_{x}^{2} + k_{y}^{2} \right)k_{z}^{2} \right/ \\ & \left[\left((1+2\epsilon)v_{p}^{2} - v_{s}^{2} \right)k_{x}^{2} + \left((1+2\epsilon)v_{p}^{2} - v_{s}^{2} \right)k_{y}^{2} + \left(v_{p}^{2} - v_{s}^{2} \right)k_{z}^{2} \right]^{2} \right\}, \end{split} \tag{A-9}$$

By performing first-order and zero-order (elliptical assumption) Taylor expansion on $\epsilon - \hat{o} = 0$ in Eq. (A-9), we can obtain the approximate eigenvalues $\lambda_{2,3}$ as

$$\begin{split} \lambda_2 &= v_{\rm p}^2 \Big[(1+2\epsilon) k_{\rm x}^2 + (1+2\epsilon) k_{\rm y}^2 + k_{\rm z}^2 \Big] + \frac{2(\delta-\epsilon) v_{\rm p}^2 \Big(v_{\rm p}^2 - v_{\rm s}^2 \Big) \Big(k_{\rm x}^2 + k_{\rm y}^2 \Big) k_{\rm z}^2}{\Big[\Big((1+2\epsilon) v_{\rm p}^2 - v_{\rm s}^2 \Big) k_{\rm x}^2 + \Big((1+2\epsilon) v_{\rm p}^2 - v_{\rm s}^2 \Big) k_{\rm y}^2 + \Big(v_{\rm p}^2 - v_{\rm s}^2 \Big) k_{\rm z}^2 \Big]}, \\ \lambda_3 &= v_{\rm s}^2 \Big[k_{\rm x}^2 + k_{\rm y}^2 + k_{\rm z}^2 \Big] - \frac{2(\delta-\epsilon) v_{\rm p}^2 \Big(v_{\rm p}^2 - v_{\rm s}^2 \Big) \Big(k_{\rm x}^2 + k_{\rm y}^2 \Big) k_{\rm z}^2}{\Big[\Big((1+2\epsilon) v_{\rm p}^2 - v_{\rm s}^2 \Big) k_{\rm x}^2 + \Big((1+2\epsilon) v_{\rm p}^2 - v_{\rm s}^2 \Big) k_{\rm y}^2 + \Big(v_{\rm p}^2 - v_{\rm s}^2 \Big) k_{\rm z}^2 \Big]}, \end{split} \tag{A-10}$$

and

$$\begin{split} \lambda_2 &= \rho v_{\rm p}^2 \Big[(1+2\epsilon) k_{\rm x}^2 + (1+2\epsilon) k_{\rm y}^2 + k_{\rm z}^2 \Big], \\ \lambda_3 &= \rho v_{\rm s}^2 \Big[k_{\rm x}^2 + k_{\rm y}^2 + k_{\rm z}^2 \Big]. \end{split} \tag{A-11} \end{split}$$

Due to the eigenvalue $\lambda = \rho^2 k^2 V^2$, we can obtain the analytical solution of phase velocities of P-, SV- and SH-waves as

expressed as

$$l = \sin(\theta)\cos(\psi),$$

$$m = \sin(\theta)\sin(\psi),$$

$$n = \cos(\theta).$$
(A-15)

where θ and ψ are the phase angles of elastic waves in the 3D space. For the horizontal interface (dip angle equals zero), they can be called incident (θ) and azimuth (ψ) angle.

$$\begin{split} V_{P} &= \text{sqrt} \bigg\{ \frac{1}{2} \left[\left((1+2\epsilon) v_{p}^{2} + v_{s}^{2} \right) l^{2} + \left((1+2\epsilon) v_{p}^{2} + v_{s}^{2} \right) m^{2} + \left(v_{p}^{2} + v_{s}^{2} \right) n^{2} \right] + \\ &\frac{1}{2} \left[\left((1+2\epsilon) v_{p}^{2} - v_{s}^{2} \right) l^{2} + \left((1+2\epsilon) v_{p}^{2} - v_{s}^{2} \right) m^{2} + \left(v_{p}^{2} - v_{s}^{2} \right) n^{2} \right] \times \\ &\text{sqrt} \bigg\{ 1 + 8 (\delta - \epsilon) v_{p}^{2} \left(v_{p}^{2} - v_{s}^{2} \right) \left(l^{2} + m^{2} \right) n^{2} \middle/ \left[\left((1+2\epsilon) v_{p}^{2} - v_{s}^{2} \right) l^{2} + \left((1+2\epsilon) v_{p}^{2} - v_{s}^{2} \right) m^{2} + \left(v_{p}^{2} - v_{s}^{2} \right) m^{2} + \left(v_{p}^{2} - v_{s}^{2} \right) m^{2} + \left(v_{p}^{2} - v_{s}^{2} \right) n^{2} \right]^{2} \bigg\} \bigg\}, \\ V_{SV} &= \text{sqrt} \bigg\{ \frac{1}{2} \left[\left((1+2\epsilon) v_{p}^{2} + v_{s}^{2} \right) l^{2} + \left((1+2\epsilon) v_{p}^{2} + v_{s}^{2} \right) m^{2} + \left(v_{p}^{2} + v_{s}^{2} \right) n^{2} \right] - \\ &\frac{1}{2} \left[\left((1+2\epsilon) v_{p}^{2} - v_{s}^{2} \right) l^{2} + \left((1+2\epsilon) v_{p}^{2} - v_{s}^{2} \right) m^{2} + \left(v_{p}^{2} - v_{s}^{2} \right) n^{2} \right] \times \\ &\text{sqrt} \bigg\{ 1 + 8 (\delta - \epsilon) v_{p}^{2} \left(v_{p}^{2} - v_{s}^{2} \right) \left(l^{2} + m^{2} \right) n^{2} \middle/ \left[\left((1+2\epsilon) v_{p}^{2} - v_{s}^{2} \right) l^{2} + \left((1+2\epsilon) v_{p}^{2} - v_{s}^{2} \right) m^{2} + \left(v_{p}^{2} - v_{s}^{2} \right) n^{2} \right]^{2} \bigg\}, \\ V_{SH} &= v_{s} \sqrt{(1+2\gamma) l^{2} + (1+2\gamma) m^{2} + n^{2}}, \end{split}$$

Substituting three solutions (Eqs. (A-12), (A-13) and (A-14)) to

$$\begin{split} V_{P} &= \text{Sqrt} \Bigg\{ v_{p}^{2} \Big[(1+2\epsilon) l^{2} + (1+2\epsilon) m^{2} + n^{2} \Big] + \frac{2(\delta-\epsilon) v_{p}^{2} \Big(v_{p}^{2} - v_{s}^{2} \Big) \Big(l^{2} + m^{2} \Big) n^{2}}{\Big[\Big((1+2\epsilon) v_{p}^{2} - v_{s}^{2} \Big) l^{2} + \Big((1+2\epsilon) v_{p}^{2} - v_{s}^{2} \Big) m^{2} + \Big(v_{p}^{2} - v_{s}^{2} \Big) n^{2} \Big]} \Bigg\}, \\ V_{SV} &= \text{Sqrt} \Bigg\{ v_{s}^{2} \Big[l^{2} + m^{2} + n^{2} \Big] - \frac{2(\delta-\epsilon) v_{p}^{2} \Big(v_{p}^{2} - v_{s}^{2} \Big) \Big(l^{2} + m^{2} \Big) n^{2}}{\Big[\Big((1+2\epsilon) v_{p}^{2} - v_{s}^{2} \Big) l^{2} + \Big((1+2\epsilon) v_{p}^{2} - v_{s}^{2} \Big) m^{2} + \Big(v_{p}^{2} - v_{s}^{2} \Big) n^{2} \Big]} \Bigg\}, \end{split}$$

$$(A-13)$$

$$V_{SH} = v_{s} \sqrt{(1+2\gamma) l^{2} + (1+2\gamma) m^{2} + n^{2}}, \end{split}$$

first-order Taylor expansion solution as

and elliptical solution as

$$\begin{split} V_{P} &= \nu_{p} \sqrt{(1+2\epsilon) l^{2} + (1+2\epsilon) m^{2} + n^{2}}, \\ V_{SH} &= \nu_{s} \sqrt{(1+2\gamma) l^{2} + (1+2\gamma) m^{2} + n^{2}}, \\ V_{SV} &= \nu_{s} \sqrt{l^{2} + m^{2} + n^{2}}. \end{split} \tag{A-14}$$

where the l, m, n represent the wave propagating direction and fulfill the relationship $k_x = kl$, $k_y = km$, $k_z = kn$, which can be

Eq. (A-4), we can obtain the unified formation polarization vectors as

$$\mathbf{D}^{P} = \begin{bmatrix} l \\ m \\ r^{p}n \end{bmatrix}, \mathbf{D}^{SV} = \begin{bmatrix} r^{sv}ln \\ r^{sv}mn \\ l^{2} + m^{2} \end{bmatrix}, \mathbf{D}^{SH} = \begin{bmatrix} m \\ -n \\ 0 \end{bmatrix}, \tag{A-16}$$

where \mathbf{D}^{P} , \mathbf{D}^{SV} and \mathbf{D}^{SH} represent the polarization of P-, SV-, and SH-wave, respectively. r is the weighted model coefficients. r^{P} and r^{SV} can be expressed with an analytical solution (Eq. (A-12)) as

$$\begin{split} r^p &= \frac{\sqrt{\left[(1+2\delta)v_p^2 - v_s^2\right]\left(v_p^2 - v_s^2\right)\left(l^2 + m^2\right)}}{f_1(\theta) - \left(v_s^2\left(l^2 + m^2\right) + v_p^2n^2\right)} \\ f_1(\theta) &= \left[\left((1+2\epsilon)v_p^2 + v_s^2\right)\left(l^2 + m^2\right) + \left(v_p^2 + v_s^2\right)n^2\right] / 2 + \left[\left((1+2\epsilon)v_p^2 - v_s^2\right)\left(l^2 + m^2\right) + \left(v_p^2 - v_s^2\right)n^2\right] / 2 \times \\ \sqrt{1 + \frac{8(\delta - \epsilon)v_p^2\left(v_p^2 - v_s^2\right)\left(l^2 + m^2\right)n^2}{\left[\left((1+2\epsilon)v_p^2 - v_s^2\right)\left(l^2 + m^2\right) + \left(v_p^2 - v_s^2\right)n^2\right]^2}}, \\ r^{sv} &= \frac{\sqrt{\left[(1+2\delta)v_p^2 - v_s^2\right]\left(v_p^2 - v_s^2\right)\left(l^2 + m^2\right)}}{f_2(\theta) - \left((1+2\epsilon)v_p^2\left(l^2 + m^2\right) + v_s^2n^2\right)} \\ f_2(\theta) &= \left[\left((1+2\epsilon)v_p^2 + v_s^2\right)\left(l^2 + m^2\right) + \left(v_p^2 + v_s^2\right)n^2\right] / 2 - \left[\left((1+2\epsilon)v_p^2 - v_s^2\right)\left(l^2 + m^2\right) + \left(v_p^2 - v_s^2\right)n^2\right] / 2 \times \\ \sqrt{1 + \frac{8(\delta - \epsilon)v_p^2\left(v_p^2 - v_s^2\right)\left(l^2 + m^2\right)n^2}{\left[\left((1+2\epsilon)v_p^2 - v_s^2\right)\left(l^2 + m^2\right) + \left(v_p^2 - v_s^2\right)n^2\right]^2}} \end{split}$$

$$r^{p} = \frac{\sqrt{\left[(1+2\delta)v_{p}^{2} - v_{s}^{2}\right]\left(v_{p}^{2} - v_{s}^{2}\right]}}{\left[(1+2\epsilon)v_{p}^{2} - v_{s}^{2}\right] + 2(\delta - \epsilon)v_{p}^{2}\left(v_{p}^{2} - v_{s}^{2}\right)n^{2} / \left[\left((1+2\epsilon)v_{p}^{2} - v_{s}^{2}\right)\left(l^{2} + m^{2}\right) + \left(v_{p}^{2} - v_{s}^{2}\right)n^{2}\right]},$$

$$\sqrt{\left[(1+2\delta)v_{p}^{2} - v_{s}^{2}\right]\left(v_{p}^{2} - v_{s}^{2}\right)}}$$

$$r^{sv} = \frac{\sqrt{\left[(1+2\delta)v_{p}^{2} - v_{s}^{2}\right]\left(v_{p}^{2} - v_{s}^{2}\right)}}{\left[v_{s}^{2} - (1+2\epsilon)v_{p}^{2}\right] - 2(\delta - \epsilon)v_{p}^{2}\left(v_{p}^{2} - v_{s}^{2}\right)n^{2} / \left[\left((1+2\epsilon)v_{p}^{2} - v_{s}^{2}\right)\left(l^{2} + m^{2}\right) + \left(v_{p}^{2} - v_{s}^{2}\right)n^{2}\right]},$$
(A-18)

and with first-order Taylor expansion solution (Eq. (A-13)) as and with zero-order Taylor expansion solution (Eq. (A-14)) as

$$r^{p} = -r^{sv} = \frac{\sqrt{\left[(1+2\delta)\nu_{p}^{2} - \nu_{s}^{2}\right]\left[\nu_{p}^{2} - \nu_{s}^{2}\right]}}{(1+2\epsilon)\nu_{p}^{2} - \nu_{s}^{2}}.$$
 (A-19)

According to Aki and Richards (2002), the elastic wave can be decomposed into P-, SV- and SH-wave modes as

$$\mathbf{u} = \mathbf{u}^{p} + \mathbf{u}^{sv} + \mathbf{u}^{sh}, \tag{A-20}$$

Substitute Eqs. (A-20) and (A-16) to Eq. (A-3) and we can obtain 3D VTI P/S wave displacement expression as

$$\mathbf{u} = A_0 \frac{\mathbf{p}^{P}}{\left|\mathbf{p}^{P}\right|} e^{-i\omega(t - \frac{1}{V_P}(xl + ym + zn))} + A_0 \frac{\mathbf{p}^{SV}}{\left|\mathbf{p}^{SV}\right|} e^{-i\omega(t - \frac{1}{V_{SV}}(xl + ym + zn))} + A_0 \frac{\mathbf{p}^{SH}}{\left|\mathbf{p}^{SH}\right|} e^{-i\omega(t - \frac{1}{V_{SH}}(xl + ym + zn))},$$
(A-21)

From Eq. (A-21) we extract the radiation patterns **RD** of P/S wave

displacement as

$$\begin{split} \mathbf{R}\mathbf{D}_{\mathrm{P}} &= \frac{\mathbf{D}^{\mathrm{P}}}{\left|\mathbf{D}^{\mathrm{P}}\right|} = \frac{(l, m, r^{\mathrm{p}} n)}{\sqrt{l^{2} + m^{2} + (r^{\mathrm{p}})^{2} n^{2}}}, \\ \mathbf{R}\mathbf{D}_{\mathrm{SV}} &= \frac{\mathbf{D}^{\mathrm{SV}}}{\left|\mathbf{D}^{\mathrm{SV}}\right|} = \frac{\left(r^{\mathrm{sv}} ln, r^{\mathrm{sv}} mn, l^{2} + m^{2}\right)}{\sqrt{\left(l^{2} + m^{2}\right)\left(l^{2} + m^{2} + (r^{\mathrm{sv}})^{2} n^{2}\right)}}, \end{split} \tag{A-22}$$

$$\mathbf{R}\mathbf{D}_{\mathrm{SH}} &= \frac{\mathbf{D}^{\mathrm{SH}}}{\left|\mathbf{D}^{\mathrm{SH}}\right|} = \frac{(m, -l, 0)}{\sqrt{l^{2} + m^{2}}}, \end{split}$$

Eq. (A-22) exhibits that the radiation patterns mainly depend on the phase angles θ and ψ and model parameters r^p and r^{sv} .

References

Aki, K., Richards, P., 2002. Quantitative Seismology. University Science Books.
Cheng, J., Fomel, S., 2014. Fast algorithms for elastic-wave-mode separation and vector decomposition using low-rank approximation for anisotropic media.
Geophysics 79, C97—C110. https://doi.org/10.1190/geo2014-0032.1.

Dellinger, J., Etgen, J., 1990. Wave-field separation in two-dimensional anisotropic media. Geophysics 55, 914–919. https://doi.org/10.1190/1.1442906.

Dou, S., Lindsey, N., Wagner, A.M., Daley, T.M., Freifeld, B., Robertson, M., Peterson, J.,

Ulrich, C., Martin, E.R., Ajo-Franklin, J.B., 2017. Distributed acoustic sensing for seismic monitoring of the near surface: a traffic-noise interferometry case study. Sci. Rep. 7, 11620–11633. https://doi.org/10.1038/s41598-017-11986-4.

- Eaid, M., Li, J., Innanen, K.A., 2018. Modeling the response of shaped DAS fibres to microseismic moment tensor sources. SEG Technical Program Expanded Abstracts, pp. 4698–4702. https://doi.org/10.1190/segam2018-2998378.1.
- Eaid, M.V., Keating, S.D., Innanen, K.A., 2020. Multiparameter seismic elastic full-waveform inversion with combined geophone and shaped fiber-optic cable data. Geophysics 85, R537–R552. https://doi.org/10.1190/geo2020-0170.1.
- Egorov, A., Correa, J., Bóna, A., Pevzner, R., Tertyshnikov, K., Glubokovskikh, S., Puzyrev, V., Gurevich, B., 2018. Elastic full-waveform inversion of vertical seismic profile data acquired with distributed acoustic sensors. Geophysics 83, R273–R281. https://doi.org/10.1190/geo2017-0718.1.
- Lellouch, A., Biondi, E., Biondi, B.L., Luo, B., Jin, G., Meadows, M.A., 2021. Properties of a deep seismic waveguide measured with an optical fiber. Phys. Rev. Res. 3 (1), 013164. https://doi.org/10.1103/PhysRevResearch.3.013164.
- Li, P., Jin, G., 2024. Using distributed acoustic sensing to characterize unconventional reservoirs via perforation-shot triggered P waves. Geophysics 89, P11–P19. https://doi.org/10.1190/geo2023-0103.1.
- Mateeva, A., Lopez, J., Potters, H., Mestayer, J., Cox, B., Kiyashchenko, D., Wills, P., Grandi, S., Hornman, K., Kuvshinov, B., Berlang, W., Yang, Z., Detomo, R., 2014. Distributed acoustic sensing for reservoir monitoring with vertical seismic profiling. Geophys. Prospect. 62, 679–692. https://doi.org/10.1111/1365-2478.12116
- Ning, I.L.C., Sava, P., 2018. Multicomponent distributed acoustic sensing: concept and theory. Geophysics 83, P1–P8. https://doi.org/10.1190/geo2017-0327.
- Rodriguez, I.V., Wuestefeld, A., 2020. Strain microseismics: radiation patterns, synthetics, and moment tensor resolvability with distributed acoustic sensing in isotropic media. Geophysics 85, KS101–KS114. https://doi.org/10.1190/geo2019-0373.1.
- Thomsen, L., 1986. Weak elastic anisotropy. Geophysics 51, 1954–1966. https://doi.org/10.1190/1.1442051.
- Tsvankin, I., 2012. Seismic Signatures and Analysis of Reflection Data in Anisotropic Media, third ed. Society of Exploration Geophysicists. https://doi.org/10.1190/1.9781560803003.
- Vavrycuk, V., 2001. Exact elastodynamic green functions for simple types of anisotropy derived from higher-order ray theory. Studia Geophys. Geod. 45,

- 67-84. https://doi.org/10.1023/A:1021754530968.
- Vavrycuk, V., 2007. Asymptotic green's function in homogeneous anisotropic viscoelastic media. Proceedings of the Royal Society A 463, 2689—2707. https:// doi.org/10.1098/rspa.2007.1862.
- Willis, M.E., 2022. Distributed Acoustic Sensing for Seismic Measurements what Geophysicists and Engineers Need to Know. Society of Exploration Geophysicists, https://doi.org/10.1190/1.9781560803850.fm.
- Yang, J., Zhang, H., Zhao, Y., Zhu, H., 2019. Elastic wavefield separation in anisotropic media based on eigenform analysis and its application in reverse-time migration. Geophys. J. Int. 217, 1290–1313. https://doi.org/10.1093/gji/gg2085.
- Zhan, G., Nahm, J., 2020. Multi-well 3D DAS VSPs: Illumination and Imaging beyond the Wellbores. In: SEG Technical Program Expanded Abstracts, pp. 3798–3802. https://doi.org/10.1190/segam2020-3426032.1.
- Zhang, L., Liu, L., Niu, F., Zuo, J., Shuai, D., Jia, W., Zhao, Y., 2022. A novel and efficient engine for p/s wave-mode vector decomposition for vti elastic reverse time migration. Geophysics 87, S185—S207. https://doi.org/10.1190/geo2021-0609.1.
- Zhang, L., Zhao, Y., Liu, L., Chen, K., Wang, Y., Zuo, J., 2023a. A fast anisotropic decoupled operator of elastic wave propagation in the space domain for p/s wave-mode decomposition and angle calculation, with its application to elastic reverse time migration in ti medium. Geophysics 88 (3), T151–T164. https://doi.org/10.1190/geo2022-0477.1.
- Zhang, L., Zhao, Y., Liu, L., Niu, F., Wang, C., Yao, Y., Li, J., Tang, H., Zuo, J., Wang, Y., 2023b. Strain Field Reconstruction from helical-winding fiber distributed acoustic sensing and its application in anisotropic elastic reverse time migration. Geophysics 89 (3), S251–S265. https://doi.org/10.1190/geo2023-0354.1.
- Zhang, L., Zhao, Y., Liu, L., Niu, F., Wu, W., Wang, C., Tang, H., Li, J., Zuo, J., Yao, Y., Wang, Y., 2024. Strain field reconstruction from helical-winding fiber distributed acoustic sensing and its application in anisotropic elastic reverse time migration. Geophysics 89, S251–S265. https://doi.org/10.1190/geo2023-0354.1.
- Zhang, Q., McMechan, G.A., 2010. 2D and 3D elastic wavefield vector decomposition in the wavenumber domain for VTI media. Geophysics 75, D13—D26. https:// doi.org/10.1190/1.3431045.
- Zuo, J., Niu, F., Liu, L., Da, S., Zhang, H., Yang, J., Zhang, L., Zhao, Y., 2022. 3D anisotropic P- and S-mode wavefields separation in 3D elastic reverse-time migration. Surv. Geophys. 43, 673–701. https://doi.org/10.1007/s10712-021-09688-8